Neutralizing the IL12/IL23 p40 Subunit Prevents Immune Checkpoint Blockade Toxicity without Compromising Antitumor Efficacy

Christianne Groeneveldt[1,2], Disha Vadgama[1,2], Anne Onrust-van Schoonhoven[1,2], Declan Whyte[1,2], Maaike M. Hofman[1,2,3], Nina E.M. Rozendaal[1,2], Menno van Nimwegen[1,2], Mike Eterman[1,2], Daphne W. Dumoulin[1,2], Ron H.J. Mathijssen[2,3], Arjen Joosse[2,3], Astrid A.M. van der Veldt[2,3,4], Louis Boon[5], Michail Doukas[6], Janneke N. Samsom[7], Ralph Stadhouders[1,2], Floris Dammeijer[1,2], Joachim G.J.V. Aerts[1,2], and Maria E. Joosse[1,2,3]

ABSTRACT

Immune checkpoint blockade (ICB) has markedly improved overall survival in various cancers but is associated with severe and sometimes fatal immune-related adverse events (irAE). Current management of irAEs involves discontinuation of ICB therapy and administration of immunosuppressive drugs, such as corticosteroids, which have been associated with decreased antitumor efficacy. Although irAE development is associated with ICB response, it is currently unknown whether their underlying mechanisms are shared or distinct. To identify early and targetable drivers of irAEs, we performed proteomic analyses on the serum of patients with cancer treated with anti–programmed cell death protein 1 (PD-1) and anti–cytotoxic T lymphocyte–associated protein 4 (CTLA-4) combination ICB. We identified a significantly increased concentration of p40, a subunit of interleukin (IL) 12/IL23, shortly after the start of ICB but before the onset of clinically apparent irAEs. Importantly, increased p40 levels were not associated with ICB efficacy. Neutralizing p40 mitigated ICB-induced toxicity in various mouse models without impairing ICB-induced antitumor efficacy. In conclusion, we demonstrated that IL12/IL23p40 is a key mediator of ICB-induced toxicity while being redundant for ICB antitumor efficacy. This shows that the mechanisms underlying ICB toxicity and efficacy can be uncoupled and provides a rationale for p40 blockade in clinical trials with ICB treatment to prevent irAEs in patients.

Introduction

Immune checkpoint blockade (ICB), which targets inhibitory receptors such as cytotoxic T lymphocyte–associated protein 4 (CTLA-4) and programmed cell death protein 1 (PD-1), has demonstrated clinical efficacy by enhancing antitumor immune responses. Currently, more than 50% of patients with metastatic cancer are eligible for ICB at any point in their treatment course, with its use extending into earlier disease settings (1). However, ICB therapy is frequently associated with immune-related adverse events (irAE), a diverse group of inflammatory toxicities arising from dysregulated immune activation that contribute to considerable morbidity and mortality (2). irAEs can affect nearly any organ system and, depending on the organ involved, cause morbidity and mortality in patients with cancer. Although some studies have reported that irAEs, particularly cutaneous and endocrine irAEs, are associated with improved overall survival, these events can also occur in patients who do not experience any clinical benefit (3–8). Furthermore, a mechanistic link between ICB efficacy and toxicity has not been demonstrated.

The current management of irAEs typically involves discontinuing ICB therapy and administering immunosuppressive drugs, including high-dose corticosteroids and, when necessary, additional systemic immunosuppressive agents to control inflammation (9). However, these interventions are not always sufficiently effective, failing to prevent irreversible organ damage or even death (10). Moreover, they carry the risk of substantial systemic side effects, and accumulating evidence suggests that beneficial antitumor immune responses elicited by ICB may be compromised (11–15). This further limits the use of ICB, particularly in patients with comorbidities or less advanced disease. Therefore, preventing rather than suppressing irAEs is a major unmet clinical need, limiting additional patient morbidity and mortality.

Previous studies have characterized peripheral blood cytokine profiles and effector T-cell signatures in affected tissues at the time of overt irAEs, identifying effector molecules associated with inflammation. In contrast, the goal of this study was to elucidate the early mechanisms that drive the development of ICB-induced toxicity, before irAEs become apparent. Specifically, we aimed to identify markers that could enable the prevention of irAEs without compromising the therapeutic efficacy of ICB. We focused on

[1]Department of Pulmonary Medicine, Erasmus University Medical Center, Rotterdam, the Netherlands. [2]Erasmus MC Cancer Institute, Erasmus University Medical Center, Rotterdam, the Netherlands. [3]Department of Medical Oncology, Erasmus University Medical Center, Rotterdam, the Netherlands. [4]Department of Radiology and Nuclear Medicine, Erasmus University Medical Center, Rotterdam, the Netherlands. [5]JJP Biologics, Warsaw, Poland. [6]Department of Pathology, Erasmus University Medical Center, Rotterdam, the Netherlands. [7]Laboratory of Pediatrics, Division Gastroenterology and Nutrition, Erasmus University Medical Center-Sophia Children's Hospital, Rotterdam, the Netherlands.

Corresponding Authors: Joachim G.J.V. Aerts, Department of Pulmonary Medicine, Erasmus MC Cancer Institute, Room Rg-436, Dr. Molewaterplein 40, Rotterdam 3015 GD, the Netherlands; E-mail: j.aerts@erasmusmc.nl; and Maria E. Joosse, Department of Pulmonary Medicine and Department of Medical Oncology, Erasmus MC Cancer Institute, Room Nt-539, Dr. Molewaterplein 40, Rotterdam 3015 GD, the Netherlands. E-mail: m.joosse@erasmusmc.nl

Cancer Immunol Res 2026;14:1731–44

doi: 10.1158/2326-6066.CIR-26-0177

This open access article is distributed under the Creative Commons Attribution-NonCommercial-NoDerivatives 4.0 International (CC BY-NC-ND 4.0) license.

©2026 The Authors; Published by the American Association for Cancer Research

anti–PD-1 and anti–CTLA-4 combination therapy, which has superior efficacy compared with monotherapy but comes at the expense of severe irAEs in up to 50% of patients, depending on the tumor type and treatment regimen (16–18). Using proteomics on serum of patients with ICB-treated melanoma who developed ICB-associated colitis and/or hepatitis, colonic tissue profiling, and complementary mouse models, we identified the interleukin (IL) 12/IL23 p40 subunit (IL23p40) as a key mediator of ICB-associated toxicity while being dispensable for its antitumor efficacy.

Materials and Methods

Study design

Two cohorts of patients with cancer were investigated in this study. Cohort I (discovery cohort) consisted of patients with metastatic melanoma ($n = 22$). In this discovery cohort, we retrospectively selected a group of patients ($n = 13$) that developed severe-grade irAEs (colitis and/or hepatitis) within the first 16 weeks of treatment, as the majority of patients develop irAEs during the first 16 weeks (2). Their irAEs were at least grade ≥2 according to the Common Terminology Criteria for Adverse Events (CTCAE) grading system and required at least 1 mg/kg/day corticosteroids for management. We also selected a group of patients ($n = 9$) who did not develop any severe-grade irAEs. However, some patients in this control group developed low-grade (CTCAE grade <2) skin toxicity more than 16 weeks after the start of ICB therapy. The patients in the two groups of the discovery cohort were matched for ICB response and several prognostic and predictive clinical parameters [age, sex, disease stage, baseline lactate dehydrogenase (LDH) levels, and *BRAF* mutation status]. Cohort II (extension cohort) consisted of patients with metastatic melanoma ($n = 9$), renal cell carcinoma (RCC; $n = 23$), and malignant mesothelioma ($n = 23$). Cohort II included patients with ICB-induced colitis or hepatitis as well as other irAEs, including nephritis, and myocarditis, myositis, and/or myasthenia. A total of 29 patients developing severe-grade irAEs requiring corticosteroids were included in the irAE group, and 26 patients who did not develop any severe-grade irAEs were included in the control group (Supplementary Table S1). For both the discovery and extension cohorts, serum samples were collected before treatment (baseline) and before the second dose of combination ICB (week 3). Importantly, at week 3, no clinical signs of toxicity were consistently documented in the irAE groups. However, because these data were collected retrospectively, milder symptoms such as pruritus may have been underreported. The best overall response, defined as the best response achieved from the start of therapy until disease progression or treatment discontinuation, was assessed according to the Response Evaluation Criteria in Solid Tumors (RECIST) version 1.1. A summary of the clinical characteristics of both cohorts is shown in Supplementary Table S1. The Medical Ethical Committee of the Erasmus University Medical Center (MC) Rotterdam, the Netherlands, approved the protocols used to collect the serum samples for this study (MULTOMAB cohort study: NL55840.078.15, MEC-2016-011; ULTIMA cohort study: NL72778.078.20, MEC-2020-0108). Written informed consent was obtained from all the patients before inclusion in the study. All procedures involving human participants were conducted in accordance with the Declaration of Helsinki and applicable national legislation.

Serum samples and protein measurements

Serum samples from patients included in the discovery cohort (cohort I) were analyzed using the SomaScan Assay v4.1 (SomaLogic Inc.), which employs 7,322 high-affinity oligonucleotide aptamers to measure 7,288 protein targets corresponding to 6,596 unique proteins, as previously described (19). The final assay readout is in relative fluorescence units, which is directly proportional to the amount of target epitope in the initial sample. Serum IL12/IL23p40, total IL12 (p70), and IL23p19 concentrations were quantified using an enzyme-linked immunosorbent assay (ELISA) for p40 (R&D Systems; #DP400), p70 (Invitrogen; #KAC1568), and p19 (R&D Systems; #D2300B). Absorbance was measured at 450 nm using a VersaMax tunable microplate reader (Molecular Devices), with background correction performed by subtracting the absorbance at 650 nm.

Single-cell RNA sequencing analysis

To identify upstream cytokine signals that drive T-cell polarization states in colonic tissues after ICB therapy, we utilized a publicly available dataset published by Luoma and colleagues (20). Here, $CD45^+$ immune cells from the colons of healthy controls (CT) and patients treated with combination therapy, who either developed colitis (C) or not (NC), were subjected to single-cell RNA sequencing (scRNA-seq) analysis. Specifically, we included patients C3, C4, C5, C6, CT1, CT2, CT3, CT4, CT6, NC1, NC2, NC4, and NC6. Patients C1, C2, and NC3 were excluded because they received anti–CTLA-4 monotherapy. Data were analyzed using Seurat v5 (21).

After excluding cells with percentage mitochondrial read counts of >5%, <200 features, or >2,500 features, 24,627 cells remained. The data were normalized and scaled using SCTranform. T-cell receptor genes (*TRAV*, *TRBV*, *TRDV*, and *TRGV* genes) and immunoglobulin variable genes (IG[A-Z]V genes) were removed from the variable features for clustering, as described by Luoma and colleagues (20). The samples were integrated with Seurat's IntegrateLayers using the HarmonyIntegration method. Principal components 1 to 30 were used for clustering at a resolution of 0.1. Clusters of $CD8^+$ and $CD4^+$ T cells were identified by their expression of CD3E and CD8A or CD4, respectively. Differentially expressed genes ($\log_2$ fold change >1; adjusted P value <0.05) were identified using FindMarkers and used as input for the Immune Response Enrichment Analysis (IREA; ref. 22).

To confirm our findings in an independent dataset, we ran IREA on differentially expressed genes previously identified by Thomas and colleagues (23). Here, $CD45^+$ immune cells from colon tissue biopsies of healthy controls ($n = 8$) and patients on ICB therapy without colitis ($n = 8$), together clustered as "controls," and patients with ICB-induced colitis ($n = 13$; "cases") were subjected to scRNA-seq and IREA as described above.

Mice

C57BL/6J mice (female, 6–8 weeks of age) were purchased from Inotiv. CBA/J mice (female, 6–8 weeks of age) were purchased from Janvier. A/JOlaHsd (A/J) mice (female, 6–8 weeks old) were purchased from Inotiv. B6.MRL-Faslpr/J (B6/lpr) mice were purchased from The Jackson Laboratory (cat. #000482) and bred in-house. Both male and female B6/lpr (6–10 weeks old) were used, and experimental groups were sex balanced.

All mice were housed under specific pathogen–free conditions in individually ventilated cages with no more than five mice/cage at the animal care facility of Erasmus MC, Rotterdam, the Netherlands. All

mouse studies were individually prepared, reviewed, approved, and registered by the Institutional Animal Welfare Body of Erasmus MC and carried out under project license AVD101002017867, issued by the central authority for scientific procedures on animals in the Netherlands ("Centrale Commissie Dierproeven"). Experiments were performed following the Dutch Act on Animal Experimentation and European Union (EU) Directive 2010/63/EU ("On the protection of animals used for scientific purposes") at the animal facility of the Erasmus MC, the Netherlands.

All experiments were initiated after at least 1 week of acclimatization following transport. Mice were randomized at the beginning of each experiment based on body weight and/or tumor volume, and the groups were randomly allocated to a treatment group. The treatments were administered in different orders each time. Body weight and tumor volumes were measured in a blinded manner concerning the treatment group, when possible.

Cell lines

The AC29 mesothelioma cell line (RRID: CVCL_4407) was derived from tumors induced by crocidolite asbestos exposure and was provided by B. W. S. Robinson (Queen Elizabeth II Medical Center, Nedlands, Australia) in 2018. AC29 cells were cultured in RPMI-1640 medium containing N-2-hydroxyethylpiperazine-N-2-ethane sulfonic acid (HEPES, 25 mmol/L; Gibco), 1% GlutaMAX (Gibco), penicillin (100 μg/mL; Gibco), streptomycin (100 μg/mL; Gibco), and 5% fetal bovine serum (FBS; Capricorn Scientific). The MC38 cell line (RRID: CVCL_B288; Kerafast, ENH204-FP) was derived from a chemically induced murine colon carcinoma. The B16.OVA cell line is a derivative of the murine melanoma cell line B16.F10 (RRID: CVCL_0159) that expresses full-length OVA protein (24). Both MC38 and B16.OVA cell lines were provided by Prof. T. van Hall (Leiden University Medical Center, Leiden, the Netherlands) in 2018 and were cultured in DMEM (Gibco) as described above with 8% FBS and further supplemented with nonessential amino acids (1×; Gibco) and sodium pyruvate (1 mmol/L; Life Technologies). The Lewis Lung Carcinoma (LLC) cell line (RRID: CVCL_4358) was kindly provided by Prof. B. Lambrecht (Vlaams Instituut voor Biotechnology, Ghent, Belgium) in 2026. MC38, B16.OVA, and LLC cells were cultured in DMEM (Gibco) as described above with 8% (MC38 and B16.OVA) or 10% (LLC) FBS and further supplemented with nonessential amino acids (1×; Gibco) and sodium pyruvate (1 mmol/L; Life Technologies). B16.OVA cells were additionally cultured with G418 (1 mg/mL; Life Technologies) and hygromycin B (60 μg/mL; Life Technologies). All cells were cultured at 37°C and 5% CO_2. Authentication of the cell lines was done by short tandem repeat profiling (IDEXX BioAnalytics). Cell lines were confirmed to be free of *Mycoplasma* by regular PCR analysis and screened for known mouse and rat pathogens using mouse/rat antibody production tests (QM Diagnostics) before *in vivo* use. Cells of low passage number were used for all experiments.

In vivo treatments

Mice received intraperitoneal injections of 200 μg anti–PD-1 (clone RMP1-14) and anti–CTLA-4 (clone UC10-4F10 or clone 9D9) every 3 days. Anti-p40 (InVivoMAb BioXcell; clone 17.8), anti-p19 (InVivoMAb BioXcell; clone G23-8), or anti-p35 (InVivoMAb BioXcell; clone C18.2) was administered intraperitoneally every 2 or 3 days (150 μg/injection), and treatment was initiated on the same day as the first anti–PD-1 and anti–CTLA-4 administration or on the day before tumor challenge. The anti–PD-1 (RMP1-14) and the anti–CTLA-4 (UC10-4F10) were kindly provided by L. Boon.

In vivo tumor models

AC29 tumors were established by intraperitoneal injection of 1×10^7 cells in 200 μL phosphate-buffered saline (PBS)/0.1% bovine serum albumin (BSA). The body circumference of mice with established intraperitoneal AC29 tumors was measured 2 to 7 times/week, and mice were euthanized when profoundly ill according to the body condition score or when body circumference reached >140% compared with baseline.

MC38, B16.OVA, or LLC tumors were inoculated via subcutaneous injection of 5×10^5 cells (MC38), 0.75×10^5 cells (B16.OVA), or 1×10^6 cells (LLC) in the right flank using 100 to 200 μL of PBS with 0.1% BSA. In cases of rechallenge in the MC38 tumor model, mice were injected subcutaneously in the opposite flank with the same number of tumor cells as in the primary tumor challenge. Tumor volumes were monitored 3 times/week using a caliper and calculated by multiplying the length, width, and height. For survival experiments, mice were euthanized when the tumor volume exceeded 1,000 mm^3 or when ulceration occurred. Therapy response was classified as progressive disease (PD), stable disease (SD; constant tumor volume for ≥7 days), partial response (PR; regression in tumor volume for ≥7 days), or complete response (CR).

For intratumoral analysis experiments, mice were sacrificed on the specified days after treatment, and tumors, spleens, tumor-draining lymph nodes (TDLN), and blood were collected. Tumors were divided into representative parts, which were either snap-frozen in liquid N_2 and stored at −80°C until further analysis, fixed in 4% formaldehyde (Carl ROTH, P087.5) for immunohistochemistry (IHC), or immediately processed into single-cell suspensions for cellular composition analysis by flow cytometry.

In vivo toxicity models

C57BL/6J mice were orally administered 3% dextran sodium sulfate (DSS; 40 kDa; TdB Labs, #DB001) in drinking water for 3 days to induce acute colitis. Additionally, mice received intraperitoneal injections of anti–PD-1 and anti–CTLA-4. Body weight was monitored daily for 7 days, and mice were euthanized when the loss of body weight reached >20% compared with baseline body weight or at the experimental endpoint on day 7. On day 7, the colon and spleen were resected to determine colon length and spleen weight. A central piece of colon tissue was fixed in 4% formaldehyde (4 hours at room temperature) and embedded in paraffin. Plasma was obtained by centrifugation of blood (15 minutes, 14,000 rpm, 4°C) and stored for further analysis.

A/J and B6/lpr mice received intraperitoneal injections of anti–PD-1 and anti–CTLA-4. At the experimental endpoint, organs were harvested for flow cytometry or fixed in 4% formaldehyde [Carl ROTH, #P087.5; 4 hours or overnight (O/N), room temperature] and embedded in paraffin.

Formalin-fixed, paraffin-embedded tissues were sectioned (4 μm) using a microtome (Microm HM 335 E) and placed on StarFrost adhesive microscope slides (Knittel Glass, #VS112751FEA.01). The slides were automatically stained with hematoxylin and eosin using a VENTANA HE 500 system (Ventana Medical Systems Inc.) according to the manufacturer's instructions and digitized using a Nanozoomer digital slide scanner (Hamamatsu Photonics) at a magnification of 40×. Using NDP.view2, a dedicated gastrointestinal (GI) pathologist

assessed colon damage and immune infiltration using a scoring system for colonic inflammation mediated by luminal antigens, as described by Erben and colleagues (25).

Fecal blood analysis

Occult blood was measured in murine stool samples using an ortho-toluidine (o-toluidine) hydrochloride test (26). In brief, stool samples were thawed, weighed, and resuspended in Milli-Q (MQ) to a final concentration of 0.25 mg/μL. The samples were centrifuged (2 minutes, 8,000 rpm, room temperature), and 20 μL of the supernatant was plated in a flat-bottom 96-well plate. A stock solution of 3% o-toluidine hydrochloride (CymitQuimica, #FT161143) in MQ was prepared, after which equal parts of the o-toluidine hydrochloride stock solution, acetic acid (Sigma-Aldrich, #A6283-1L), and 100% ethanol (VWR Chemicals, #20821.330) were mixed to obtain an o-toluidine hydrochloride working solution. Next, four parts of the o-toluidine hydrochloride working solution were mixed with one part of 6% H_2O_2. Subsequently, 50 μL of this solution was added to the stool supernatant. The emergence of a green color indicated a positive hemoccult, and positive samples were identified in a blinded manner by an independent scientist.

LEGENDplex

The concentrations of chemokines (Cxcl9 and Cxcl10) and cytokines [GM-CSF, IFNα, IFNβ, IFNγ, IL1β, IL6, IL12/IL23p40, IL12p70, IL23p19, and tumor necrosis factor (TNF) α] in murine plasma samples were measured using the LEGENDplex Mouse Cytokine 2 V02 Panel (#741334) and the Mouse Cytokine Release Syndrome Panel (#741024, BioLegend). The procedure was executed following the manufacturer's instructions, with the modification that samples were incubated with the mixed beads O/N at 4°C before the addition of detection antibodies. Samples were acquired using a FACSymphony A5 (BD Biosciences) and analyzed using BioLegend's LEGENDplex Data Analysis Software.

IHC

Sections were deparaffinized and rehydrated, and endogenous peroxidase activity was quenched using 1.5% H_2O_2 (Merck, #1.07210) in PBS (20 minutes, room temperature). Heat-mediated antigen retrieval was performed using 0.1 mol/L citric acid (Sigma-Aldrich, C1909) with 0.1 mol/L sodium citrate (Merck, #1.06448) in distilled water (10 minutes). Nonspecific binding was blocked using SuperBlock (Thermo Fisher Scientific, #37580) for 1 hour at room temperature before incubation with a rat anti–mouse CD8a antibody (Invitrogen, #14-0808-82, clone 4SM15; 1:1,600, O/N, 4°C) in PBS/1% BSA. Samples were then incubated for 60 minutes at room temperature with a biotinylated donkey anti-rat antibody (Jackson ImmunoResearch, #712-065-153, 1:150 in PBS), followed by incubation with an avidin–biotin complex (VECTASTAIN Elite ABC HRP Kit; Vector Labs, #PK-6101) for 30 minutes at room temperature. Peroxidase activity was detected using 0.5 mg/mL 3,3-diaminobenzidine tetrahydrochloride (DAB; Thermo Fisher Scientific, #J6221606) in 30 mmol/L imidazole (Merck, #8.14223) with 1 mmol/L ethylenediaminetetraacetic acid (EDTA, Merck, #1.08418), and 0.0003% H_2O_2 (Sigma-Aldrich, #216763; 20 minutes, room temperature in the dark). Slides were counterstained with hematoxylin (Vector Labs, #H-3401) for 1 second, dehydrated, and mounted using Entellan (Sigma-Aldrich, #1.07961.0500).

The sections were digitized using a Nanozoomer digital slide scanner (Hamamatsu Photonics) at a magnification of 40×. $CD8^+$ T lymphocytes were quantified using QuPath (v0.5) through automated positive cell detection on bright-field images using the hematoxylin optical density (OD) channel. The detection parameters, including a pixel size of 0.3 μm, an object area range of 5 to 600 μm^2, and a single-threshold classifier for DAB mean OD (threshold = 0.1566), were optimized on a representative region of interest. All other detection parameters were maintained at default settings. These optimized settings were then uniformly applied across all sections using a custom QuPath script. Cell counts were exported for downstream analysis using GraphPad Prism (v8.0).

Flow cytometry

Single-cell suspensions were generated from isolated blood, spleen, bronchoalveolar lavage (BAL), TDLNs, heart, liver, and tumor tissue. Briefly, blood was collected in EDTA tubes (Microvette CB300, Sarstedt) and lysed for 10 minutes at room temperature by erythrocyte lysis using osmotic lysis buffer (8.3% NH_4Cl, 1% $KHCO_3$, and 0.04% Na_2EDTA in MQ). Single-cell suspensions of spleens, livers, and lymph nodes were generated by mechanical dispersion through a 70-μm nylon mesh cell strainer (Falcon, #352350), followed by osmotic lysis of erythrocytes in the spleen and liver suspensions. Tumors and hearts were collected and dissociated using a validated tumor dissociation kit (Miltenyi Biotec, #130-096-730), according to the manufacturer's protocol. After dissociation, the samples were mechanically dispersed through a 70-μm nylon mesh cell strainer, and erythrocytes were lysed in the heart suspensions.

Single-cell suspensions were incubated with eBioscience Fixable Viability Dye eFluor 506 (Invitrogen, #65-0866-14) in PBS for 20 minutes at room temperature. If applicable, the cells were incubated with PE-conjugated H-$2K^b$ $Rpl18_{119–126}$ tetramers [generated as described previously using the KILTFDRL peptide (27)] for 30 minutes at room temperature in 30 μL FACS buffer (PBS, 0.5% BSA, and 1% sodium azide). After tetramer incubation, antibodies for surface markers (Supplementary Table S2) were added directly to the tetramer mixture in 10 μL of Brilliant Stain buffer (Thermo Fisher Scientific, #00-4409-42) and incubated for 30 minutes at room temperature. If applicable, cells were fixed and permeabilized for intracellular marker staining (Supplementary Table S2) using the FoxP3/Transcription Factor Staining Buffer Set (Thermo Fisher Scientific, #00-5523-00) according to the manufacturer's protocol. Finally, the cells were resuspended in FACS buffer, filtered, and acquired using FACSymphony A5 (BD Biosciences). Data were analyzed using FlowJo software v.10.8.1 (Tree Star) and OMIQ software according to the gating strategy shown in Supplementary Fig. S1.

Statistics and reproducibility

Statistical analyses were performed using GraphPad Prism (v8). Differences between patient groups were determined using the Mann–Whitney U test for continuous variables and the Fisher exact test for categorical outcomes. To compare IL12p40 concentrations in human serum at baseline versus week 3, two-way analysis of variance (ANOVA) with the Šidák multiple comparisons test was used. Differences in absolute changes in serum IL12/IL23p40 levels were analyzed using an unpaired *t* test with Welch correction. For murine data, differences between two groups were assessed using an ordinary one-way ANOVA with the Dunnett or Tukey multiple

comparisons test or a Kruskal–Wallis test with the Dunn *post hoc* test. Changes in body weight or tumor growth over time were statistically assessed using a two-way ANOVA with the Dunnett multiple comparisons test. Survival was evaluated using the Kaplan–Meier method, and significant differences were calculated using the Mantel–Cox log-rank test. Data are shown as the mean ± SEM, and statistical significance was set at $P < 0.05$.

Results

Early increase in IL12/IL23p40 associates with irAE development in patients with cancer

To identify mediators of irAE pathogenesis in patients, we performed proteomics (SomaScan, $n = 6{,}596$ proteins) on the serum samples of patients with metastatic melanoma, collected before and 3 weeks after the first dose of anti–PD-1 and anti–CTLA-4 combination therapy (nivolumab and ipilimumab; **Fig. 1A**). In this discovery cohort, one group of patients ($n = 13$) developed irAEs (colitis and/or hepatitis) within the first 16 weeks of treatment. The median time to irAE onset was 44 days following the initiation of ICB therapy. These irAEs necessitated the discontinuation of ICB therapy and administration of high-dose corticosteroids (classified as grade ≥2 according to the CTCAE grading system and requiring at least 1 mg/kg/day corticosteroids for management). This group was matched based on several clinical parameters (i.e., age, sex, disease stage, baseline LDH levels, and *BRAF* mutation status) to a control group of patients ($n = 9$) who did not experience severe-grade irAEs within the first 16 weeks of treatment (Supplementary Table S1). At baseline, serum proteome analysis identified no relevant immunologic differences between patients with and without irAEs (Supplementary Fig. S2; Supplementary Table S3; ref. 28). However, at week 3, there were marked differences in the accumulation of numerous immune-related proteins between the two groups (**Fig. 1B**). The specific proteins and pathways associated with irAE development at week 3 in this discovery cohort were different from those associated with the ICB treatment response (Supplementary Fig. S3A–S3C), suggesting that toxicity and efficacy may arise through distinct mechanisms. One of the most notable changes was a marked increase in IL12/IL23p40 (also known as IL12B) levels at week 3, specifically in the serum of patients who would later develop irAEs (Supplementary Table S3; **Fig. 1B** and **C**).

To further substantiate the potential relevance of p40 in irAE development, we performed IREA (22) using data from two published scRNA-seq analyses of ICB-induced colitis biopsies from patients with cancer (20, 23). From both datasets, we extracted genes that were differentially expressed in colonic T cells from patients with ICB-associated colitis compared with those from patients without colitis. In both independent datasets, IREA identified IL12 as one of the most prominent cytokines predicted to drive these irAE-associated transcriptional changes in $CD8^+$ (**Fig. 1D** and **E**) and $CD4^+$ (Supplementary Fig. S4A and S4B) colonic T cells, suggesting a potential involvement of IL12 signaling in the development of GI irAEs.

Based on these findings, we prioritized IL12/IL23p40 for further validation. To investigate whether our SomaScan results were specific for the p40 subunit or for total IL12 (IL12p70, consisting of IL12p40 and IL12p35) or IL23 proteins (consisting of p40 with its alternative binding partner IL23p19), we performed targeted ELISAs. This analysis confirmed a specific increase in the p40 subunit (**Fig. 1F**) but not total IL12 or IL23 in the serum of patients with ICB-induced irAEs (Supplementary Table S4). In patients who developed irAEs, p40 concentrations at week 3 were significantly elevated, with a 3.6-fold increase compared with baseline levels (from 88.58 pg/mL at baseline to 290.92 pg/mL at week 3; $P = 0.002$). In contrast, patients who did not develop irAEs showed only a modest, nonsignificant increase in p40 levels (from 62.95 pg/mL at baseline to 126.86 pg/mL at week 3; $P = 0.626$).

The accumulation of p40 was not restricted to GI irAEs or patients with melanoma, as analysis of an extended cohort revealed increased serum p40 concentrations in ICB-treated patients who developed other irAEs, including nephritis, myositis, myocarditis, and/or myasthenia (103.1 pg/mL at baseline versus 201.0 pg/mL at week 3; $P < 0.0001$; **Fig. 1G**; Supplementary Fig. S5A). The increase was also observed in patients with malignancies other than melanoma, including malignant mesothelioma and RCC, despite differences in ICB dosing and treatment schedules (Supplementary Fig. S5B). Overall, all evaluated patients with irAEs showed a significantly higher absolute increase in IL12/IL23p40 levels compared with control patients (**Fig. 1H**).

Serum p40 levels were increased both in responders (CR, PR, and SD) and nonresponders (PD), suggesting that, in this cohort, an increase in the p40 concentration is not a general feature of ICB treatment but is instead specifically associated with the development of ICB-related toxicity (Supplementary Fig. S6A and S6B). Therefore, we selected this cytokine subunit for further functional characterization and neutralization experiments.

p40 neutralization prevents ICB-induced toxicity

To investigate whether p40 can cause irAE development, we examined whether p40-neutralizing antibodies prevented ICB-induced colitis in an ICB-aggravated DSS-induced colitis mouse model that mimics intestinal irAEs in patients (29). Seven days after the start of treatment, we assessed various parameters for colitis severity, including weight loss, presence of fecal blood, and colon length (**Fig. 2A**). The addition of p40-neutralizing antibodies largely prevented weight loss in this model (**Fig. 2B** and **C**), as did the neutralization of IL12p35 (Supplementary Fig. S7A–S7D). In contrast, IL23p19 neutralization did not prevent weight loss, indicating that IL12 rather than IL23 contributed to the development of ICB-induced colitis (**Fig. 2B** and **C**). In line with earlier observations (29), the addition of ICB did not further enhance DSS-induced weight loss, but ICB administration enhanced plasma levels of proinflammatory cytokines, including type I IFNs (IFNα/β), IL1β, IL6, and TNFα, compared with mice treated with DSS only (**Fig. 2D**; Supplementary Table S5). This is particularly relevant, as many of these cytokines are currently individually targeted as second- or third-line treatments in corticosteroid-resistant irAEs (9), suggesting that blocking p40 could have a more widespread and upstream effect in preventing irAE development. Locally in the colon, p40 neutralization showed a trend toward a reduction in ICB-induced intestinal pathology, as evidenced by a lower incidence of intestinal blood loss (**Fig. 2E**), decreased colonic shortening (**Fig. 2F**), and reduced histologic inflammation scores, as blindly assessed by a GI pathologist (**Fig. 2G** and **H**).

To assess whether p40 neutralization could decrease ICB-induced inflammation in organs other than the colon, we treated autoimmune-prone B6/lpr mice (30) and wild-type (WT) A/J mice (31) with a combination of ICB with or without anti-p40 (**Fig. 2I**). In B6/lpr mice, we observed that anti-p40 treatment negated the ICB-induced induction of systemic inflammatory cytokines

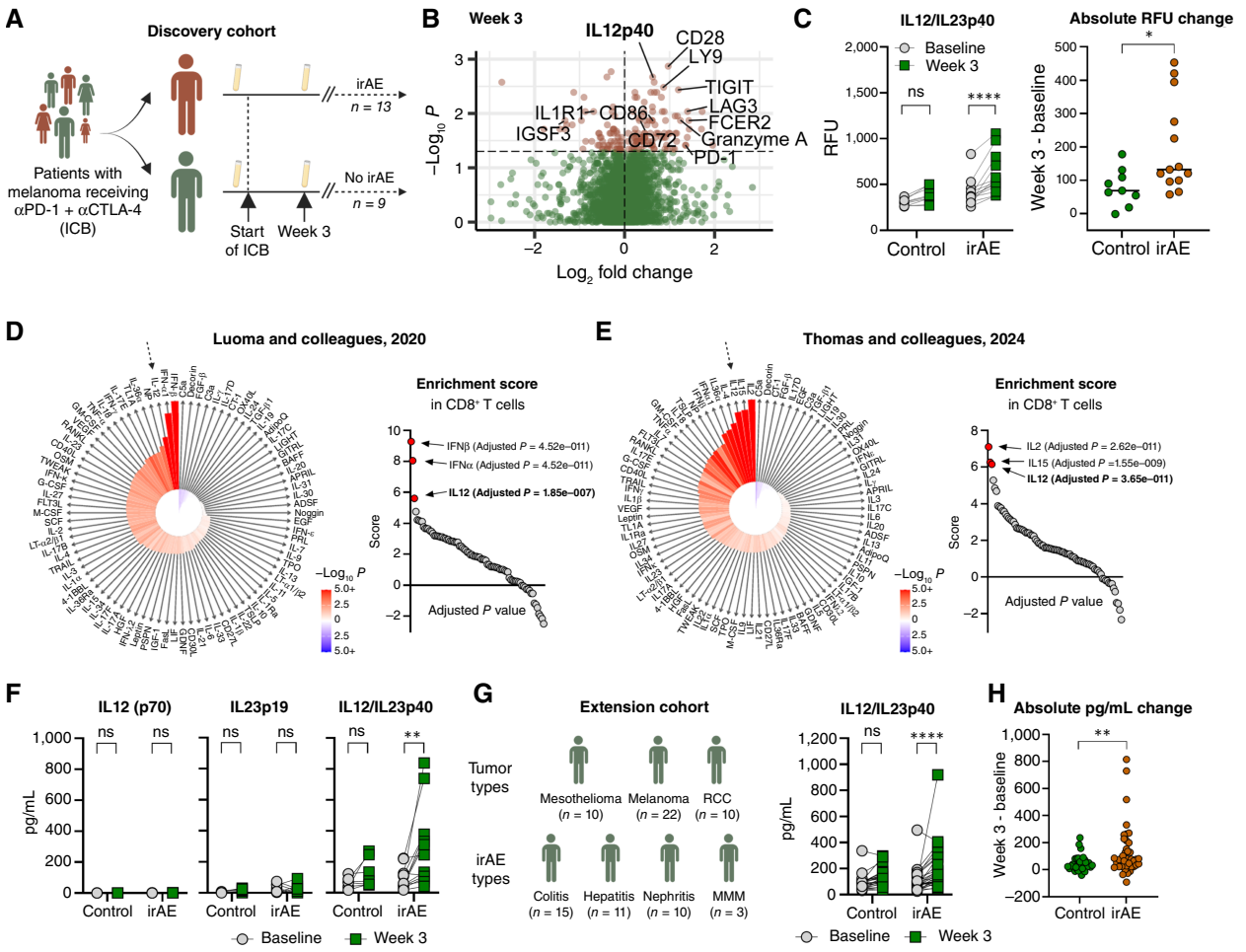


Figure 1.

Early accumulation of IL12/IL23p40 associates with irAE development in patients with cancer. **A,** Description of the discovery patient cohort and timepoints when serum was collected for SomaScan proteomic analysis. Serum of patients with melanoma was collected before (baseline) and 3 weeks after the start of immunotherapy, prior to irAE (immunotherapy-related colitis and/or hepatitis) development. **B,** Volcano plot displaying proteins with increased serum abundance in patients developing irAEs after ICB (week 3). **C,** IL12/IL23p40 relative fluorescence units (RFU) prior to (circles) and after (squares) immunotherapy in control patients and patients developing irAEs and absolute change in RFU. **D** and **E,** IREA output on publicly available scRNA-seq data from CD8$^+$ T cells in ICB-induced colitis biopsies relative to non-colitis biopsies. **F,** Total IL12 protein (p70), IL23p19, and IL12/IL23p40 subunit serum levels as measured by ELISA from the initial cohort. **G,** IL12/IL23p40 serum levels measured by ELISA in the extension cohort. **H,** Absolute change in serum IL12/IL23 concentration (pg/mL) in discovery and extension cohorts. Differences between groups were determined using a two-way ANOVA with the Dunnett multiple comparisons test (**C**, **F**, and **G**) or an unpaired *t* test with Welch correction (**C** and **H**). *, $P < 0.05$; **, $P < 0.01$; ****, $P < 0.0001$; ns, not significant. αCTLA-4, anti–CTLA-4; αPD-1, anti–PD-1; MMM, myocarditis, myositis, and/or myasthenia. [**A,** Created in BioRender. Groeneveldt, C. (2026) https://BioRender.com/o9ofygv; **G,** Created in BioRender. Groeneveldt, C. (2026) https://BioRender.com/2m9fykb.]

(**Fig. 2J**). We also observed an ICB-induced increase in CD3$^+$ T cells in the BAL and liver, indicative of pneumonitis and hepatitis, which was mitigated by p40 neutralization (**Fig. 2K**). Similarly, in A/J mice, the ICB-induced induction of systemic inflammatory cytokines was mitigated by p40 neutralization (**Fig. 2L**). Additionally, p40 neutralization decreased the ICB-induced activation, proliferation, and memory T-cell expansion of CD3$^+$ T cells in the peripheral blood (**Fig. 2M**) and BAL (**Fig. 2N**). Other organs were minimally or not affected by ICB with or without p40 neutralization in both mouse models (Supplementary Fig. S8A and S8B). Collectively, these data show that early blockade of p40 during irAE development can mitigate ICB-induced systemic inflammation and reduce organ-specific toxicity in multiple irAE models.

The induction of tumor-specific immune responses by ICB therapy is preserved upon p40 neutralization

To enable the safe and preemptive use of p40 neutralization in patients eligible to receive ICB, it is essential that ICB-induced antitumor immunity remains intact. Therefore, we assessed the effect of p40 neutralization on the antitumor efficacy of ICB in the ICB-induced colitis mouse model, in which WT C57BL/6J mice were additionally engrafted with subcutaneous MC38 murine colon carcinoma tumors (**Fig. 3A**). Due to the discomfort caused by DSS, we monitored tumor growth for a maximum of 40 days. Similar to non–tumor-bearing mice in earlier experiments, neutralizing p40 prevented DSS + ICB–induced weight loss (**Fig. 3B**). Importantly, antitumor immunity, as measured by the induction of MC38-directed Rpl18 tumor antigen–specific

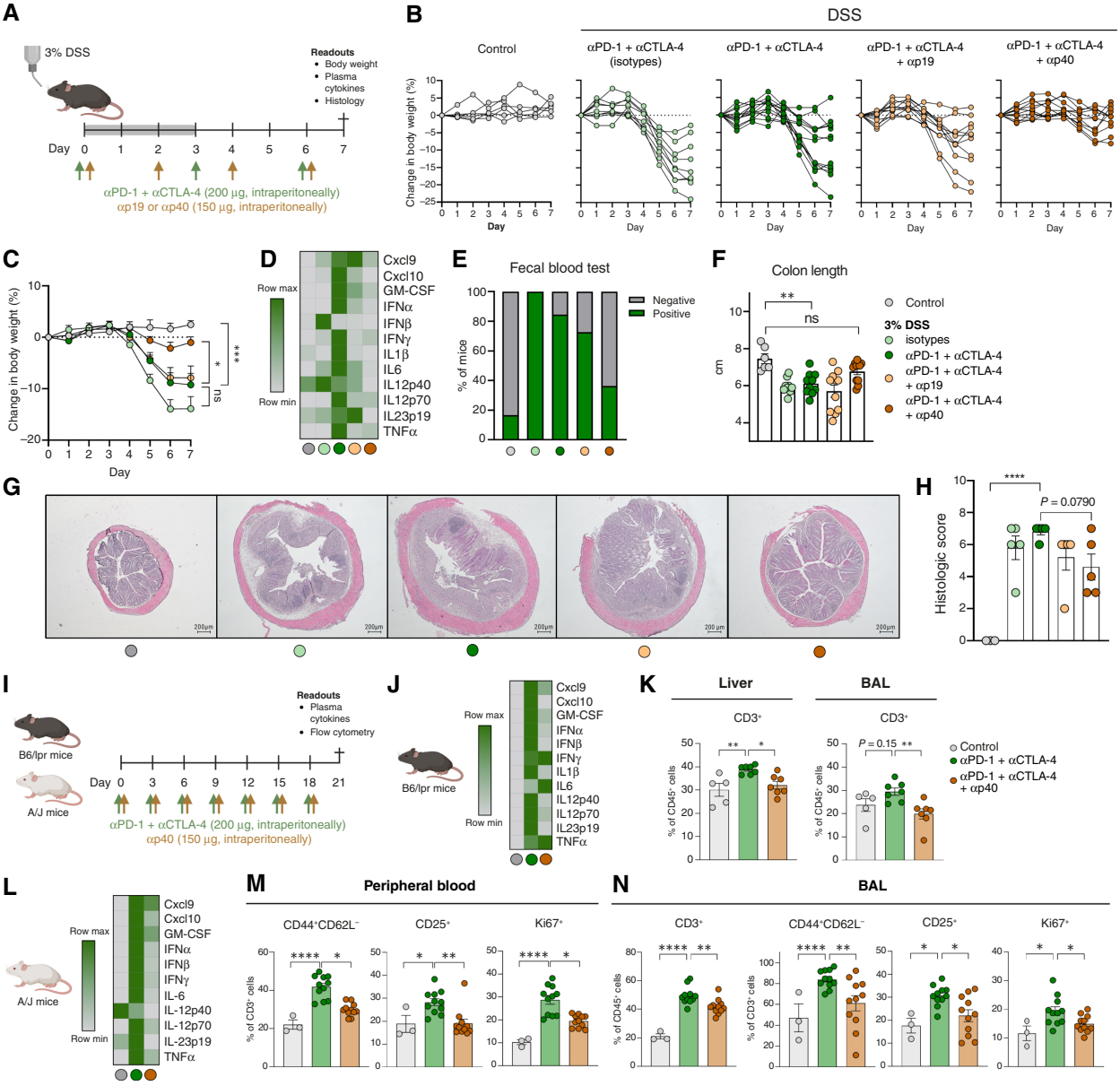


Figure 2.

p40 neutralization mitigates ICB-induced toxicity in multiple irAE models. **A,** Overview of experiment described in **B–H**. DSS (3%) was added to the drinking water of female C57BL/6J mice ($n = 6$–13/group, combination of 2 experiments) for 3 days, and mice received intraperitoneal injections with anti–PD-1 (αPD-1; 200 μg), anti–CTLA-4 (αCTLA-4; 200 μg), anti-p19 (αp19; 150 μg), or anti-p40 (αp40; 150 μg) on indicated days. **B,** Changes in bodyweight of individual mice compared with baseline (day 0). **C,** Average change in bodyweight per experimental group. **D,** Cytokine levels in plasma, measured by LEGENDplex. **E,** Percentage of mice with the positive or negative fecal blood test. **F,** Colon length on day 7. **G,** Representative images of colons harvested on day 7, stained with hematoxylin and eosin (H&E). Scale bars, 200 μm. **H,** Quantification of histologic scores, as determined by a licensed pathologist based on H&E-stained colon sections. **I,** Overview of experiment described in **J–N**. Male and female B6/lpr mice ($n = 5$–7/group) or female WT A/J mice ($n = 3$–11/group) were intraperitoneally injected on indicated days with αPD-1 + αCTLA-4, with or without αp40. **J,** Cytokine levels in plasma of B6/lpr mice on day 21, measured by LEGENDplex. **K,** Frequency of $CD3^+$ T cells in the liver or BAL of B6/lpr mice after indicated therapies. **L,** Cytokine levels in plasma of A/J mice on day 21, measured by LEGENDplex. **M** and **N,** Frequency, activation, proliferation, and memory T-cell expansion of $CD3^+$ T cells in peripheral blood (**M**) and BAL (**N**) of A/J mice after indicated therapies. Differences between groups were determined using a two-way ANOVA (**C**) or an ordinary one-way ANOVA with the Dunnett (**F**, **K**, **M**, and **N**) or Holm–Šidák (**H**) multiple comparisons test. Data represent mean ± SEM. *, $P < 0.05$; **, $P < 0.01$; ***, $P < 0.001$; ****, $P < 0.0001$; ns, not significant. [**A,** Created in BioRender. Groeneveldt, C. (2026) https://BioRender.com/takky0b; **I, J,** and **L,** Created in BioRender. Groeneveldt, C. (2026) https://BioRender.com/64e3f40.]

$CD8^+$ T cells in peripheral blood, was comparable in mice receiving ICB with or without p40-neutralizing antibodies (**Fig. 3C**). These observations coincided with similar tumor outgrowth and survival in this short-term experiment (**Fig. 3D–F**), indicating that p40 neutralization can selectively prevent ICB-induced toxicity without decreasing antitumor efficacy.

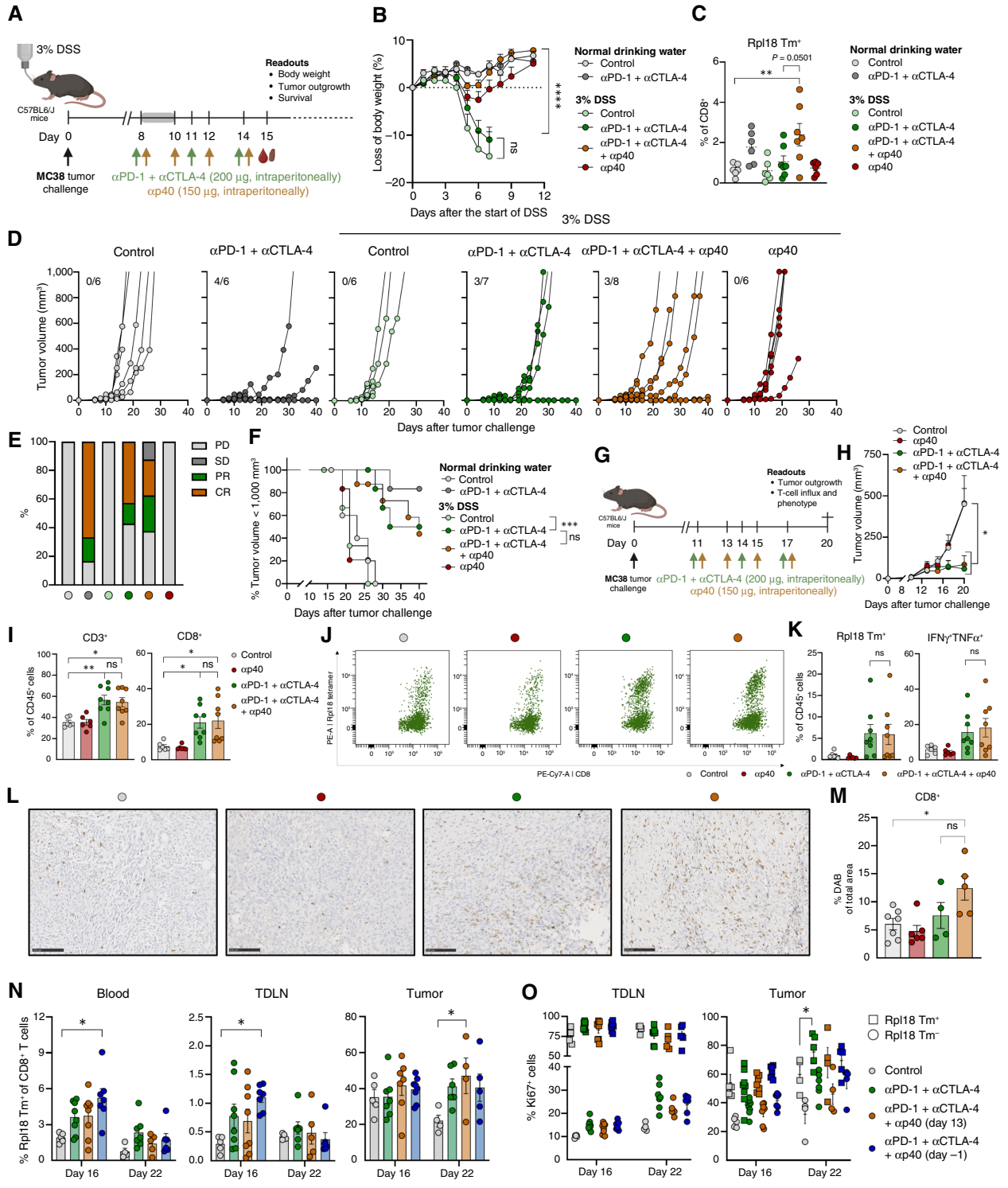


Figure 3.

p40 neutralization preserves the induction of tumor-specific immune responses by ICB therapy. **A,** Overview of the experiment described in **B–G**. The experiment was executed as described in **Fig. 2A**, and female C57BL/6J mice (n = 6–8/group) were additionally challenged subcutaneously with 5×10^5 MC38 tumor cells. Tumor outgrowth was measured 3 times/week, and mice were euthanized at the end of the experiment (day 40) or when one of the following humane endpoints occurred: loss of body weight >20%, tumor volume >1,000 mm^3, or ulceration of the tumor. **B,** Average change in body weight. **C,** Frequency of circulating $CD8^+$ Rpl18 tetramer $(Tm)^+$ T cells. **D,** Individual tumor growth curves of mice receiving indicated therapies. **E,** Frequency of mice with no response, SD, PR, or CR within each treatment group. **F,** Kaplan–Meier survival curves of mice after indicated treatments. (*Continued on the following page.*)

To further demonstrate that p40 neutralization does not inhibit the induction of tumor-specific T-cell responses, we assessed the frequency of T cells in tumors following combined ICB therapy and p40 neutralization, as well as their local and systemic specificity, frequency, and phenotype (**Fig. 3G**). ICB therapy again delayed tumor outgrowth (**Fig. 3H**) and promoted intratumoral infiltration of tumor-specific and functional $CD8^+$ T cells, which was preserved in the context of p40 neutralization (**Fig. 3I–M**). In addition, the proportion of $IFN\gamma^+TNF\alpha^+$ T cells among the total $CD45^+$ tumor-infiltrating cells was comparable between mice treated with anti-p40 and those receiving ICB alone, consistent with intact Th1-type differentiation and effector polarization. T-cell proliferation and activation in the blood, spleen, TDLNs, and tumor were increased after ICB therapy and maintained by additional p40 blockade (Supplementary Fig. S9A–D).

To understand the impact of p40 on the kinetics of T-cell activation, we repeated the experiment with analyses after the first and third ICB doses and initiated p40 neutralization either at the start of ICB therapy (day 13) or before tumor challenge (day −1; Supplementary Fig. S9E). Following the first ICB dose (day 16), an increase in tumor-specific $CD8^+$ T cells was observed in peripheral blood and TDLNs, and this increase was evident in the tumor after the third ICB dose (day 22; **Fig. 3N**). The frequency, the proliferative potential, and the effector phenotype of intratumoral T cells were not mitigated by p40 neutralization, both when initiated concurrently with ICB or before the tumor challenge (**Fig. 3O**; Supplementary Fig. S9F). This suggests that p40 is not required for the initial priming of endogenous antitumor immunity. Substituting the non–regulatory T cell (Treg)–depleting anti–CTLA-4 clone (UC10-4F10-11) with the Treg-depleting clone 9D9 also did not result in any negative impact of p40 neutralization (Supplementary Fig. S10). Collectively, these data demonstrate that p40 can be neutralized without compromising antitumor T-cell immunity.

Anti-p40 does not compromise the efficacy of anti–PD-1 and/or anti–CTLA-4 therapy in multiple tumor models

To validate the results described above for other tumor types in which combination ICB is clinically applied and to assess the effects of anti-p40 on long-term survival, we employed the poorly immunogenic LLC tumor model, the partially sensitive B16.OVA murine melanoma model, and the ICB-responsive orthotopic AC29 mesothelioma model. In the LLC tumor model (**Fig. 4A**), p40 neutralization did not affect the moderate, short-term reduction in tumor growth induced by ICB therapy, as reflected by similar tumor volumes between treatment groups (**Fig. 4B**). However, due to the rapid, aggressive outgrowth of LLC tumors, both ICB and ICB in combination with anti-p40 provided no survival benefit (**Fig. 4C**). In the B16.OVA model (**Fig. 4D**), ICB therapy induced a delay in tumor outgrowth (**Fig. 4E**) and moderately improved survival, which was not impaired when p40 neutralization was added (**Fig. 4F**). ICB-induced T-cell proliferation and activation did not decrease when ICB therapy was combined with anti-p40, suggesting that p40 was dispensable for antitumor T-cell activation in this model (**Fig. 4G**). Treatment of AC29 mesothelioma–bearing mice (**Fig. 4H**) with ICB reduced ascites accumulation (**Fig. 4I**) and significantly improved survival (**Fig. 4J**), effects that were not altered by the addition of anti-p40 antibodies. Altogether, these results from different tumor subtypes at varying anatomic locations show that p40 can be safely blocked without compromising antitumor immunity.

To determine whether the effect of p40 neutralization during ICB therapy depends on the type of an ICB regimen, we assessed antitumor efficacy in the context of both ICB monotherapy and combination therapy in the MC38 model (**Fig. 5A**). Although anti–CTLA-4 monotherapy was ineffective in limiting MC38 tumor progression, anti–PD-1 therapy showed efficacy (Supplementary Fig. S11) but to a lesser extent than the combination ICB treatment. This is consistent with clinical trial data from patients with various malignancies, including microsatellite-instable colorectal cancer (32). Again, anti-p40 did not perturb the antitumor efficacy of ICB, both when administered as anti–PD-1 and anti–CTLA-4 combination therapy or as anti–PD-1 monotherapy (**Fig. 5B–E**). To investigate whether long-term responses to tumor antigens were preserved in the context of IL12p40 inhibition, we rechallenged all surviving mice with MC38 tumor cells. In contrast to tumor-naïve mice, all mice that cleared the primary tumor also rejected an MC38 rechallenge (**Fig. 5F**), suggesting the induction of effective and durable memory T-cell responses. Taken together, our data demonstrate that p40 neutralization does not impair the efficacy of ICB monotherapy or combination therapy, including the establishment of tumor-specific memory responses.

Discussion

By leveraging proteomic profiling of patient serum collected shortly after the initiation of ICB therapy (anti–CTLA-4 and anti–PD-1) but before the onset of clinically manifest irAEs, we identified the p40 subunit of IL12/IL23 as an upstream cytokine driving irAE development. Using different clinically relevant tumor models and organ-specific and multiorgan ICB toxicity models, we showed that neutralizing p40 mitigated ICB-induced toxicity without reducing antitumor efficacy. Taken together, our findings identify IL12 as a key mediator of ICB-induced toxicity while being redundant for

(*Continued.*) **G,** Overview of experiment described in **H–M**. Female C57BL/6J mice ($n = 6$–8/group) were subcutaneously challenged with 5×10^5 MC38 tumor cells and received indicated treatments. **H,** Average tumor volumes. **I,** Intratumoral frequency of $CD3^+$ or $CD8^+$ T cells within the $CD45^+$ immune cell population. **J,** Scatterplots displaying the presence of tumor-specific Rpl18 Tm^+ T cells within tumors of each experimental group. From each tumor sample, 250 $CD8^+$ T cells were subsampled to allow objective comparison. **K,** Intratumoral frequency of Rpl18 Tm^+ or $IFN\gamma^+TNF\alpha^+$ T cells within the $CD45^+$ immune cell population. **L,** Representative images obtained from IHC staining of MC38 tumors for CD8; scale bars, 100 μm. **M,** Quantification of intratumoral $CD8^+$ T cells in all evaluable tumors. **N,** Frequency of Rpl18 Tm^+ $CD8^+$ T cells in blood, TDLNs, and tumors. Female C57BL/6J mice ($n = 4$–8/group) were inoculated with MC38 tumors as described in (**G**), and ICB was administered on days 13, 16, and 19. Anti-p40 was administered every 2 days, starting at day −1 or day 13. **O,** Percentage of Ki67 expression in Rpl18 Tm^+ or Tm^- 20 $CD8^+$ T cells in the TDLNs and tumor. Differences between groups were determined using a two-way ANOVA (**B**, **H**, **N**, and **O**) or an ordinary one-way ANOVA with the Tukey multiple comparisons test (**C**, **I**, and **M**) or a Kruskal–Wallis test with the Dunn multiple comparisons test (**K**). Log-rank tests were used to compare differences in survival in (**F**). Data represent mean ± SEM. *, $P < 0.05$; **, $P < 0.01$; ***, $P < 0.001$; ****, $P < 0.0001$; ns, not significant. αCTLA-4, anti–CTLA-4; αPD-1, anti–PD-1; αp40, anti-p40. [**A,** Created in BioRender. Groeneveldt, C. (2026) https://BioRender.com/d3ey8x6; **G,** Created in BioRender. Groeneveldt, C. (2026) https://BioRender.com/78g4p8o.]

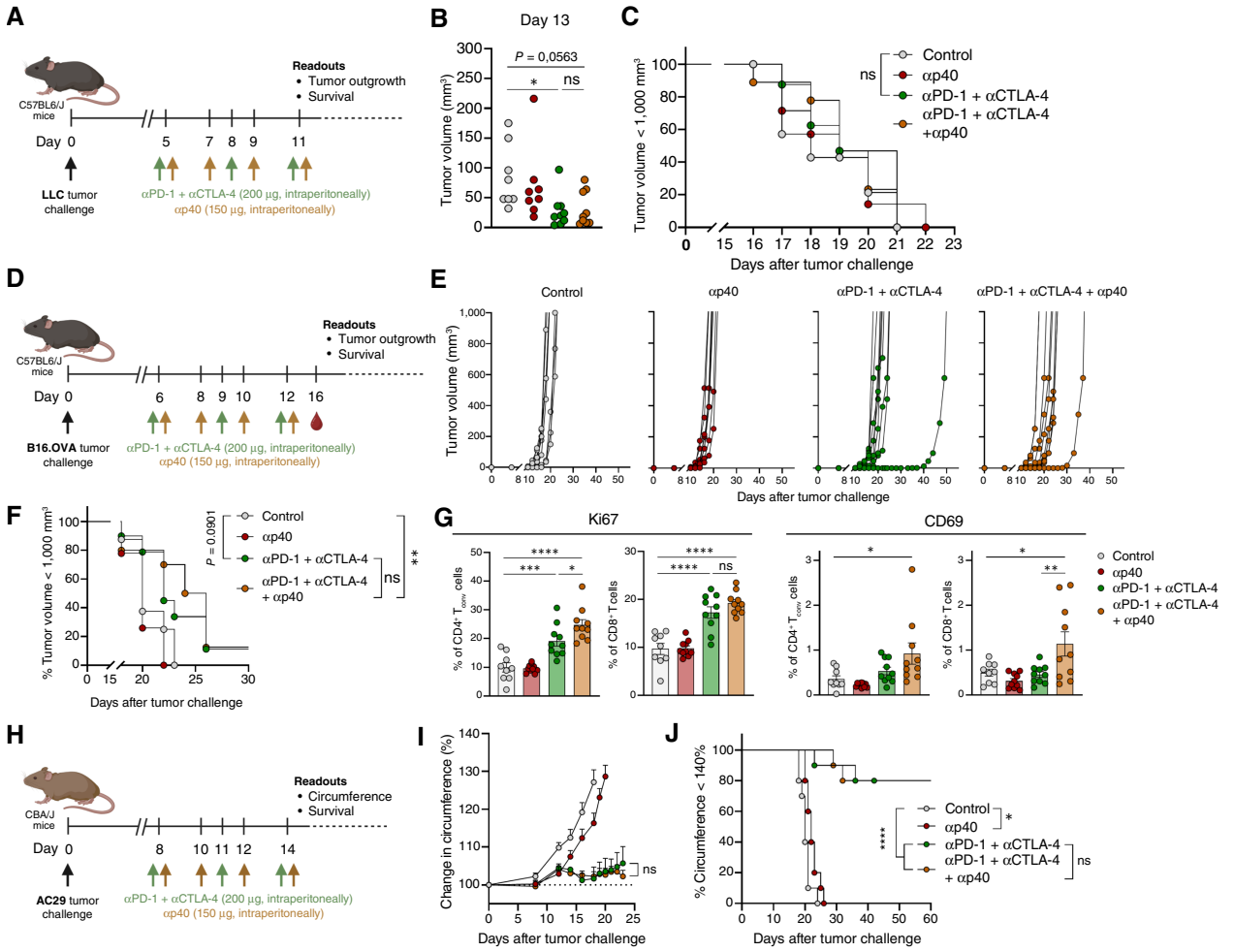


Figure 4.

Efficacy of ICB therapy is maintained following p40 neutralization across multiple preclinical models. **A,** Overview of the experiment described in (**B**) and (**C**). Female C57BL/6J mice ($n = 8$–9/group) were challenged subcutaneously with 1×10^6 LLC tumor cells and received indicated treatments. Tumor outgrowth was monitored 3–7 times/week. **B,** Tumor volumes on day 13 after tumor challenge. **C,** Kaplan–Meier survival curves of LLC-bearing mice after indicated treatments. **D,** Overview of the experiment described in (**E–G**). Female C57BL/6J mice ($n = 10$/group) were challenged subcutaneously with 0.75×10^5 B16.OVA tumor cells and received indicated treatments. Tumor outgrowth was monitored 3 times/week. **E,** Individual tumor growth curves of mice receiving indicated therapies. **F,** Kaplan–Meier survival curves of B16.OVA-bearing mice after indicated treatments. **G,** Frequency of $Ki67^+$ or $CD69^+CD4^+$ or $CD8^+$ T cells in the circulation on day 16. **H,** Overview of the experiment described in (**I**) and (**J**). Female CBA/J mice ($n = 10$/group) were challenged intraperitoneally with 10×10^6 AC29 tumor cells and received indicated treatments. Waist circumference (as a proxy for ascites production and tumor growth) was measured every 1–2 days. **I,** Average change in waist circumference. **J,** Kaplan–Meier survival curves of AC29-bearing mice after indicated treatments. Differences between groups were determined using an ordinary one-way ANOVA with the Šídák multiple comparisons test (**B** and **G**), a two-way ANOVA (**I**), or log-rank tests (**C**, **F**, and **I**). Data represent mean ± SEM. *, $P < 0.05$; **, $P < 0.01$; ***, $P < 0.001$; ****, $P < 0.0001$; ns, not significant. αCTLA-4, anti–CTLA-4; αPD-1, anti–PD-1; αp40, anti-p40. [**A,** Created in BioRender. Groeneveldt, C. (2026) https://BioRender.com/fzgkv72; **D,** Created in BioRender. Groeneveldt, C. (2026) https://BioRender.com/d1dsxxc; **H,** Created in BioRender. Groeneveldt, C. (2026) https://BioRender.com/vemgl0v.]

antitumor efficacy, highlighting it as a promising therapeutic target for translation into a phase I/II clinical trial.

Patients who develop irAEs have consistently been shown to experience better outcomes compared with those who do not, although this association varies according to the severity of the toxicity. Low-grade irAEs are more consistently associated with improved survival, whereas severe irAEs often require ICB discontinuation and administration of high-dose corticosteroids (5–9, 33, 34). Importantly, evidence across multiple tumor types suggests that high-dose corticosteroid use may attenuate the survival benefit associated with ICB (11–15), even after adjusting for irAE severity and type (35). These observations highlight the need for therapeutic strategies that limit corticosteroid exposure, underscoring the importance of identifying actionable drivers of irAEs that may enable the uncoupling of toxicity from antitumor efficacy. In this context, p40 emerged as a promising candidate, as explored in this study.

How can systemic p40 mediate local irAE development? The p40 subunit is known to be present at significantly higher concentrations in human serum than biologically active IL12 and IL23 heterodimers, especially during inflammation (36). In addition to IL12 being produced within a single cell, recent evidence supports

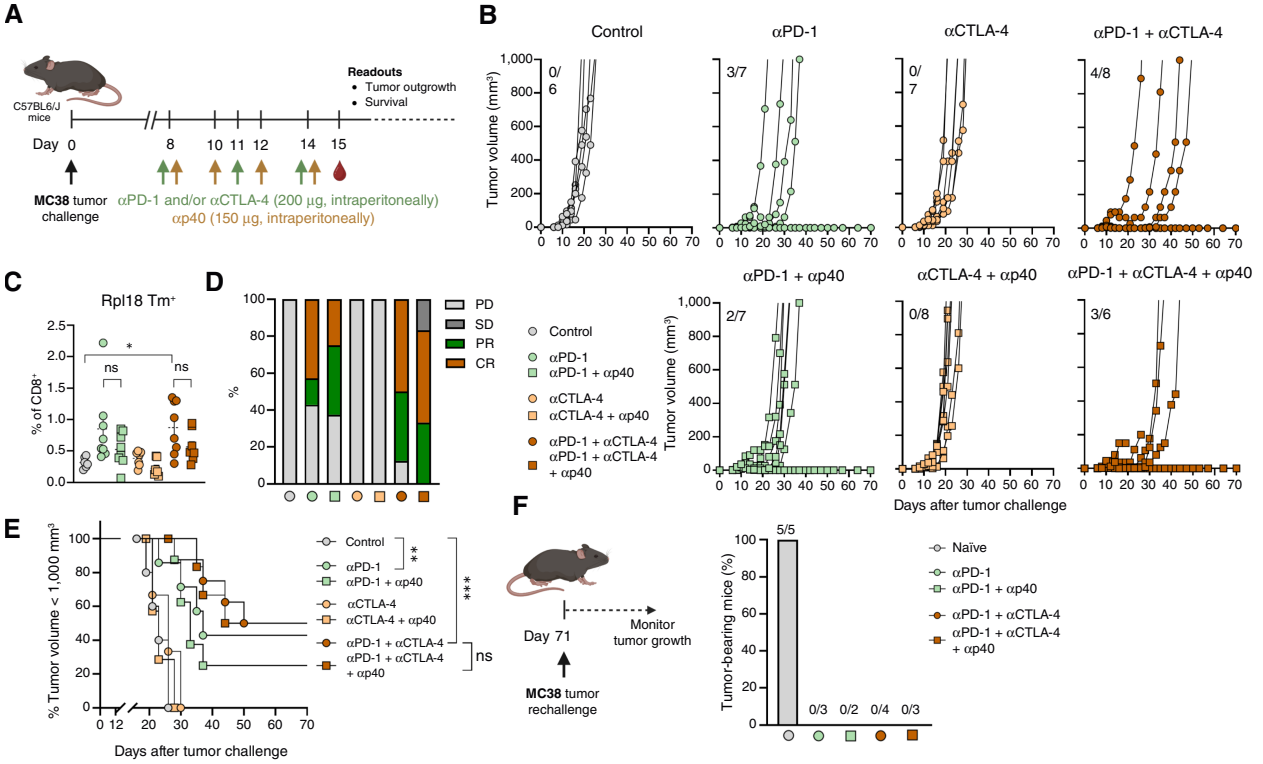


Figure 5.

p40 neutralization does not compromise the efficacy of monotherapy or combination ICB therapy. **A,** Overview of the experiment described in **B–F**. Female C57BL/6J mice (n = 6–8/group) were challenged subcutaneously with 5×10^5 MC38 tumor cells and received indicated treatments. Tumor outgrowth was measured 3 times/week. **B,** Individual tumor growth curves of mice receiving indicated therapies. **C,** Frequency of circulating $CD8^+$ Rpl18 tetramer $(Tm)^+$ T cells on day 15. **D,** Frequency of mice with no response, SD, PR, or CR within each treatment group. **E,** Kaplan–Meier survival curves of mice after indicated treatments. **F,** Rechallenge experiment. All CR mice from (**D**) were subcutaneously engrafted with 5×10^5 MC38 tumor cells in the alternate flank on day 71, and tumor outgrowth was measured 3 times/week. Number of tumor-bearing mice within each group. Differences between groups were determined using an ordinary one-way ANOVA with the Tukey multiple comparisons test (**C**) or log-rank tests (**E**). Data represent mean ± SEM. *, $P < 0.05$; **, $P < 0.01$; ***, $P < 0.001$; ns, not significant. αCTLA-4, anti–CTLA-4; αPD-1, anti–PD-1; αp40, anti-p40. [**A,** Created in BioRender. Groeneveldt, C. (2026) https://BioRender.com/xy8xsas; **F,** Created in BioRender. Groeneveldt, C. (2026) https://BioRender.com/t2dmtrx.]

a "two-cell" model in which circulating p40 monomers can extracellularly bind p35, leading to functional IL12 formation *in vivo* in a tissue-localized manner, without both subunits needing to be present in the same cell (37, 38). In the context of irAEs, an early increase in circulating p40 after the start of ICB treatment may result in heterodimerization with locally expressed p35, enabling IL12 formation within specific tissue microenvironments. This could indicate that the local tissue environment of a particular organ sculpts the onset and site of irAE development following increased systemic p40 levels in susceptible patients, a hypothesis that requires further evaluation.

IL12 plays a well-established role in promoting antitumor immunity. The therapeutic administration of IL12 in tumors has been extensively studied, often showing an additional benefit when combined with ICB at the expense of increased toxicity (39, 40). However, it remains uncertain whether endogenous IL12p40 is truly essential for the development of antitumor responses, as shown by conflicting results between studies (41–43). Building on these existing findings, our data demonstrated that IL12 is not required for the efficacy of ICB or intratumoral cytokine production both during tumor initiation and in established disease, the latter better reflecting the clinical setting. One potential explanation for these observations could be that blockade of p40 may be functionally compensated by other cytokines, such as IL18, which can also support IFNγ production and cytotoxic T-cell activity in the absence of IL12 (44, 45). Notably, although IL12 has been reported to exert antiangiogenic effects, these are largely mediated through IFNγ-dependent mechanisms (46), which seem preserved in our models, suggesting that local antiangiogenic activity is unlikely to be substantially impaired by p40 blockade. In addition, IL23 and Th17 cells have been implicated in tumor progression and metastasis in some cancers. Blocking IL23 through p40 neutralization could therefore offer potential benefits in a tumor setting (41, 47). Further studies are necessary to dissect the exact molecular and cellular mechanisms underlying this redundancy and to clarify the context-dependent role of IL12p40 in antitumor immunity. Taken together, despite the pleiotropic roles of IL12, p40-targeted strategies represent a viable and promising approach to uncouple toxicity from efficacy during ICB therapy.

Several case reports have described the use of anti-p40 antibodies to successfully treat already apparent, mostly corticosteroid-refractory colitis in ICB-treated patients (48, 49). Based on these observations and our findings, we propose the design and implementation of a phase I/II clinical trial to evaluate the preemptive use of an approved anti-p40 monoclonal antibody in patients initiating dual ICB (e.g., ipilimumab and nivolumab) or other treatment combinations. Ideally, such a trial would target a tumor type with high ICB-related toxicity, but modest

response rates, such as mesothelioma, to evaluate whether p40 blockade can reduce irAE incidence without diminishing antitumor efficacy. Antibodies targeting p40 are already FDA-approved and widely used in the treatment of autoimmune diseases, including inflammatory bowel disease and psoriasis. Treatment with anti-p40 is not typically associated with an increased risk of serious infections, distinguishing them from other immunosuppressive agents (50). This supports their potential repurposing to prevent and reduce irAEs in the context of cancer immunotherapy while preserving antitumor immunity.

Notably, p40 blockade differs mechanistically from TNF or IL6 inhibition, which have also shown efficacy in reducing ICB-associated toxicity (29, 51). TNF and IL6 are downstream effector cytokines produced after immune activation, and their inhibition is typically applied once inflammatory responses are established. In contrast, p40 acts upstream by regulating T-cell differentiation and expansion. Preemptive targeting of p40 may therefore limit the differentiation of pathogenic T-cell responses before tissue damage occurs. This upstream mode of action suggests that anti-p40 therapy could represent a more preventive strategy to mitigate irAEs while preserving antitumor immunity.

This study has several limitations. First, we focused on patients developing severe-grade irAEs; however, because irAEs were assessed retrospectively, additional low-grade irAEs may have been present in both the irAE and control groups due to underreporting, potentially contributing to the heterogeneity observed in p40 levels. With regard to our mouse studies, mice are generally resistant to the development of ICB-induced irAEs, and we therefore employed a combination of models, including chemically induced organ damage and genetically autoimmune-prone strains, to investigate the impact of p40 neutralization on irAE development. In line with the original report (29), ICB did not exacerbate DSS-induced weight loss in our study. The original study reported increased colonic wall thickening as assessed by ultrasound as a measure of increased colonic damage following ICB, which was not evaluated in our experimental setup; a comparable effect in our study therefore cannot be excluded. Similar to TNFα inhibition used in the original report (29, 52), p40 inhibition attenuated DSS-induced weight loss, suggesting that these effects may be mediated, at least in part, through modulation of baseline inflammatory responses. In B6/lpr mice and WT A/J mice, we observed less pronounced histologic inflammation as was reported in previous studies (30, 31). This is a common problem in studies investigating ICB-induced toxicity and may be attributable to differences in housing conditions, microbiome composition, or other environmental factors. The use of other genetically engineered models [such as CTLA-$4^{+/-}$/PD-$1^{-/-}$ knockout mice (53)] could further strengthen the preclinical evaluation of p40-neutralizing antibodies in irAE development.

In conclusion, the identification of IL12/IL23p40 as a key mediator of ICB-induced toxicity, while being redundant for antitumor efficacy bridges a critical gap in cancer immunotherapy, offering an approach to managing irAEs while maintaining the robust antitumor responses that make ICB therapy so revolutionary.

Data Availability

All data are available in the main text or supplementary material.

Authors' Disclosures

D.W. Dumoulin reports personal fees from MSD, Amgen, Roche, Pfizer, Accord Healthcare, Bristol Myers Squibb, and AstraZeneca outside the submitted work. R.H.J. Mathijssen reports grants from Astellas, Bayer, Boehringer Ingelheim, Deuteroncology, Nordic Pharma, Novartis, Pamgene, Pfizer, Roche, Sanofi, and Servier outside the submitted work. A.A.M. van der Veldt reports other support from Bristol Myers Squibb, Sanofi, Regeneron, Novartis, Pierre Fabre, Ipsen, and GE HealthCare outside the submitted work. L. Boon reports other support from JJP Biologics during the conduct of the study; other support from JJP Biologics outside the submitted work; and a patent for Anti-human HVEM (TNFRSF14) Antibodies and Uses Thereof pending and issued. F. Dammeijer reports a patent for P37412NL00 issued. J.G.J.V. Aerts reports personal fees from MSD, Eli Lilly and Company, Amphera, Accord Healthcare, and Summit Therapeutics and grants and personal fees from AstraZeneca and Nutricia outside the submitted work, as well as a patent for Allogeneic Tumor Cell Lysate licensed to Amphera and a patent for P37412NL00 issued. M.E. Joosse reports grants from Dutch Research Council (ZonMw) during the conduct of the study, as well as a patent for P37412NL00 issued. No disclosures were reported by the other authors.

Authors' Contributions

C. Groeneveldt: Data curation, formal analysis, investigation, visualization, methodology, writing–original draft, project administration, writing–review and editing. **D. Vadgama:** Formal analysis, investigation, visualization, writing–review and editing. **A. Onrust-van Schoonhoven:** Investigation, writing–review and editing. **D. Whyte:** Investigation. **M.M. Hofman:** Investigation, writing–review and editing. **N.E.M. Rozendaal:** Investigation, writing–review and editing. **M. van Nimwegen:** Investigation, writing–review and editing. **M. Eterman:** Investigation, writing–review and editing. **D.W. Dumoulin:** Resources, writing–review and editing. **R.H.J. Mathijssen:** Resources, writing–review and editing. **A. Joosse:** Resources, writing–review and editing. **A.A.M. van der Veldt:** Resources, writing–review and editing. **L. Boon:** Resources, writing–review and editing. **M. Doukas:** Investigation, writing–review and editing. **J.N. Samsom:** Resources, writing–review and editing. **R. Stadhouders:** Methodology, writing–review and editing. **F. Dammeijer:** Conceptualization, methodology, writing–review and editing. **J.G.J.V. Aerts:** Conceptualization, supervision, funding acquisition, writing–review and editing. **M.E. Joosse:** Conceptualization, data curation, formal analysis, supervision, funding acquisition, investigation, visualization, methodology, writing–original draft, project administration, writing–review and editing.

Acknowledgments

The authors would like to thank all those who contributed to the successful completion of this research. The authors are particularly grateful to Mandy van Gulijk, Farzana Mohammad, Githangely St. Hilaire, Jennifer Schipper-van Hulst, and Zahra Khalajzeyqami for their technical assistance during mouse experiments and Danielle Hulleman-van Haaften and Lisette van Berkel for providing protocols and sharing their expertise in using DSS to induce intestinal inflammation. R. Stadhouders is supported by the European Molecular Biology Organization (EMBO) Young Investigator Program (project number 5868) and a Dutch Research Council (ZonMw) Vidi grant (09150172010068). M.E. Joosse is supported by the Dutch Research Council (ZonMw) Veni grant (09150162410045).

Note

Supplementary data for this article are available at Cancer Immunology Research Online (http://cancerimmunolres.aacrjournals.org/).

Received February 9, 2026; revised June 19, 2026; accepted August 28, 2026; posted first August 31, 2026.

References

1. Haslam A, Gill J, Prasad V. Estimation of the percentage of US patients with cancer who are eligible for immune checkpoint inhibitor drugs. JAMA Netw Open 2020;3:e200423. https://doi.org/10.1001/jamanetworkopen.2020.0423.

2. Martins F, Sofiya L, Sykiotis GP, Lamine F, Maillard M, Fraga M, et al. Adverse effects of immune-checkpoint inhibitors: epidemiology, management and surveillance. Nat Rev Clin Oncol 2019;16:563–80. https://doi.org/10.1038/s41571-019-0218-0.

3. Amoroso V, Gallo F, Alberti A, Paloschi D, Ferrari Bravo W, Esposito A, et al. Immune-related adverse events as potential surrogates of immune checkpoint inhibitors' efficacy: a systematic review and meta-analysis of randomized studies. ESMO Open 2023;8:100787. https://doi.org/10.1016/j.esmoop.2023.100787.
4. Shankar B, Zhang J, Naqash AR, Forde PM, Feliciano JL, Marrone KA, et al. Multisystem immune-related adverse events associated with immune checkpoint inhibitors for treatment of non-small cell lung cancer. JAMA Oncol 2020;6:1952–6. https://doi.org/10.1001/jamaoncol.2020.5012.
5. Eggermont AMM, Kicinski M, Blank CU, Mandala M, Long GV, Atkinson V, et al. Association between immune-related adverse events and recurrence-free survival among patients with stage III melanoma randomized to receive pembrolizumab or placebo: a secondary analysis of a randomized clinical trial. JAMA Oncol 2020;6:519–27. https://doi.org/10.1001/jamaoncol.2019.5570.
6. Wan G, Chen W, Khattab S, Roster K, Nguyen N, Yan B, et al. Multi-organ immune-related adverse events from immune checkpoint inhibitors and their downstream implications: a retrospective multicohort study. Lancet Oncol 2024;25:1053–69. https://doi.org/10.1016/s1470-2045(24)00278-x.
7. Zhong L, Wu Q, Chen F, Liu J, Xie X. Immune-related adverse events: promising predictors for efficacy of immune checkpoint inhibitors. Cancer Immunol Immunother 2021;70:2559–76. https://doi.org/10.1007/s00262-020-02803-5.
8. Fan Y, Xie W, Huang H, Wang Y, Li G, Geng Y, et al. Association of immune related adverse events with efficacy of immune checkpoint inhibitors and overall survival in cancers: a systemic review and meta-analysis. Front Oncol 2021;11:633032. https://doi.org/10.3389/fonc.2021.633032.
9. Haanen J, Obeid M, Spain L, Carbonnel F, Wang Y, Robert C, et al. Management of toxicities from immunotherapy: ESMO Clinical Practice Guideline for diagnosis, treatment and follow-up. Ann Oncol 2022;33:1217–38. https://doi.org/10.1016/j.annonc.2022.10.001.
10. Wang DY, Salem JE, Cohen JV, Chandra S, Menzer C, Ye F, et al. Fatal toxic effects associated with immune checkpoint inhibitors: a systematic review and meta-analysis. JAMA Oncol 2018;4:1721–8. https://doi.org/10.1001/jamaoncol.2018.3923.
11. Verheijden RJ, de Groot JS, Fabriek BO, Hew MN, May AM, Suijkerbuijk KPM. Corticosteroids for immune-related adverse events and checkpoint inhibitor efficacy: analysis of six clinical trials. J Clin Oncol 2024;42:3713–24. https://doi.org/10.1200/jco.24.00191.
12. Faje AT, Lawrence D, Flaherty K, Freedman C, Fadden R, Rubin K, et al. High-dose glucocorticoids for the treatment of ipilimumab-induced hypophysitis is associated with reduced survival in patients with melanoma. Cancer 2018;124:3706–14. https://doi.org/10.1002/cncr.31629.
13. van Dijk EJ, Smeenk MM, Bensch F, Sadowska AM, Verschueren MV, Verhaert M, et al. Checkpoint inhibitor effectiveness after corticosteroids and second-line immunosuppressants for immune-related adverse events in non-small-cell lung cancer. ESMO Open 2026;11:106052. https://doi.org/10.1016/j.esmoop.2025.106052.
14. Bai X, Hu J, Betof Warner A, Quach HT, Cann CG, Zhang MZ, et al. Early use of high-dose glucocorticoid for the management of irAE is associated with poorer survival in patients with advanced melanoma treated with anti-PD-1 monotherapy. Clin Cancer Res 2021;27:5993–6000. https://doi.org/10.1158/1078-0432.Ccr-21-1283.
15. Curkovic NB, Irlmeier R, Bai X, Cui C, Ye F, Burnette HR, et al. Impact of steroid dose and timing on efficacy of combination PD-1/CTLA-4 blockade. Oncoimmunology 2025;14:2494433. https://doi.org/10.1080/2162402x.2025.2494433.
16. Larkin J, Chiarion-Sileni V, Gonzalez R, Grob JJ, Cowey CL, Lao CD, et al. Combined nivolumab and ipilimumab or monotherapy in untreated melanoma. N Engl J Med 2015;373:23–34. https://doi.org/10.1056/NEJMoa1504030.
17. Baas P, Scherpereel A, Nowak AK, Fujimoto N, Peters S, Tsao AS, et al. First-line nivolumab plus ipilimumab in unresectable malignant pleural mesothelioma (CheckMate 743): a multicentre, randomised, open-label, phase 3 trial. Lancet 2021;397:375–86. https://doi.org/10.1016/s0140-6736(20)32714-8.
18. Motzer RJ, Tannir NM, McDermott DF, Arén Frontera O, Melichar B, Choueiri TK, et al. Nivolumab plus ipilimumab versus sunitinib in advanced renal-cell carcinoma. N Engl J Med 2018;378:1277–90. https://doi.org/10.1056/NEJMoa1712126.
19. Gold L, Ayers D, Bertino J, Bock C, Bock A, Brody EN, et al. Aptamer-based multiplexed proteomic technology for biomarker discovery. PLoS One 2010;5:e15004. https://doi.org/10.1371/journal.pone.0015004.
20. Luoma AM, Suo S, Williams HL, Sharova T, Sullivan K, Manos M, et al. Molecular pathways of colon inflammation induced by cancer immunotherapy. Cell 2020;182:655–71.e22. https://doi.org/10.1016/j.cell.2020.06.001.
21. Hao Y, Stuart T, Kowalski MH, Choudhary S, Hoffman P, Hartman A, et al. Dictionary learning for integrative, multimodal and scalable single-cell analysis. Nat Biotechnol 2024;42:293–304. https://doi.org/10.1038/s41587-023-01767-y.
22. Cui A, Huang T, Li S, Ma A, Pérez JL, Sander C, et al. Dictionary of immune responses to cytokines at single-cell resolution. Nature 2024;625:377–84. https://doi.org/10.1038/s41586-023-06816-9.
23. Thomas MF, Slowikowski K, Manakongtreecheep K, Sen P, Samanta N, Tantivit J, et al. Single-cell transcriptomic analyses reveal distinct immune cell contributions to epithelial barrier dysfunction in checkpoint inhibitor colitis. Nat Med 2024;30:1349–62. https://doi.org/10.1038/s41591-024-02895-x.
24. Schuurhuis DH, van Montfoort N, Ioan-Facsinay A, Jiawan R, Camps M, Nouta J, et al. Immune complex-loaded dendritic cells are superior to soluble immune complexes as antitumor vaccine. J Immunol 2006;176:4573–80. https://doi.org/10.4049/jimmunol.176.8.4573.
25. Erben U, Loddenkemper C, Doerfel K, Spieckermann S, Haller D, Heimesaat MM, et al. A guide to histomorphological evaluation of intestinal inflammation in mouse models. Int J Clin Exp Pathol 2014;7:4557–76.
26. Wahba N. An ortho-tolidine hydrochloride test for the detection of occult blood in faeces without dietary restrictions. J Clin Pathol 1965;18:687–8. https://doi.org/10.1136/jcp.18.5.687.
27. Ruibal P, Franken K, van Meijgaarden KE, Walters LC, McMichael AJ, Gillespie GM, et al. Discovery of HLA-E-presented epitopes: MHC-E/peptide binding and T-cell recognition. Methods Mol Biol 2022;2574:15–30. https://doi.org/10.1007/978-1-0716-2712-9_2.
28. Zhou Y, Zhou B, Pache L, Chang M, Khodabakhshi AH, Tanaseichuk O, et al. Metascape provides a biologist-oriented resource for the analysis of systems-level datasets. Nat Commun 2019;10:1523. https://doi.org/10.1038/s41467-019-09234-6.
29. Perez-Ruiz E, Minute L, Otano I, Alvarez M, Ochoa MC, Belsue V, et al. Prophylactic TNF blockade uncouples efficacy and toxicity in dual CTLA-4 and PD-1 immunotherapy. Nature 2019;569:428–32. https://doi.org/10.1038/s41586-019-1162-y.
30. Adam K, Iuga A, Tocheva AS, Mor A. A novel mouse model for checkpoint inhibitor-induced adverse events. PLoS One 2021;16:e0246168. https://doi.org/10.1371/journal.pone.0246168.
31. Won T, Kalinoski HM, Wood MK, Hughes DM, Jaime CM, Delgado P, et al. Cardiac myosin-specific autoimmune T cells contribute to immune-checkpoint-inhibitor-associated myocarditis. Cell Rep 2022;41:111611. https://doi.org/10.1016/j.celrep.2022.111611.
32. André T, Elez E, Lenz HJ, Jensen LH, Touchefeu Y, Van Cutsem E, et al. Nivolumab plus ipilimumab versus nivolumab in microsatellite instability-high metastatic colorectal cancer (CheckMate 8HW): a randomised, open-label, phase 3 trial. Lancet 2025;405:383–95. https://doi.org/10.1016/s0140-6736(24)02848-4.
33. Li Y, Zhang Y, Jia X, Jiang P, Mao Z, Liang T, et al. Effect of immune-related adverse events and pneumonitis on prognosis in advanced non-small cell lung cancer: a comprehensive systematic review and meta-analysis. Clin Lung Cancer 2021;22:e889–900. https://doi.org/10.1016/j.cllc.2021.05.004.
34. Zhang S, Tang K, Wan G, Nguyen N, Lu C, Ugwu-Dike P, et al. Cutaneous immune-related adverse events are associated with longer overall survival in advanced cancer patients on immune checkpoint inhibitors: a multi-institutional cohort study. J Am Acad Dermatol 2023;88:1024–32. https://doi.org/10.1016/j.jaad.2022.12.048.
35. Verheijden RJ, de Groot JS, Fabriek BO, Hew MN, May AM, Suijkerbuijk KPM. Reply to: peak corticosteroid dose for immune-related adverse events and survival: not the whole story. J Clin Oncol 2025;43:616–19. https://doi.org/10.1200/jco-24-02234.
36. Gately MK, Renzetti LM, Magram J, Stern AS, Adorini L, Gubler U, et al. The interleukin-12/interleukin-12-receptor system: role in normal and pathologic immune responses. Annu Rev Immunol 1998;16:495–521. https://doi.org/10.1146/annurev.immunol.16.1.495.
37. Gerber AN, Abdi K, Singh NJ. The subunits of IL-12, originating from two distinct cells, can functionally synergize to protect against pathogen dissemination in vivo. Cell Rep 2021;37:109816. https://doi.org/10.1016/j.celrep.2021.109816.
38. Abdi K, Singh NJ, Spooner E, Kessler BM, Radaev S, Lantz L, et al. Free IL-12p40 monomer is a polyfunctional adaptor for generating novel IL-12-like heterodimers extracellularly. J Immunol 2014;192:6028–36. https://doi.org/10.4049/jimmunol.1400159.

39. Jiang Z, Yang N, Jin J, Zhang Z, Lu H, Xu L, et al. Preclinical and clinical evaluation of intratumoral injection of an IL-12 expressing SKV-012 oncolytic virus for advanced solid tumors. J Immunother Cancer 2025;13:e011642. https://doi.org/10.1136/jitc-2025-011642.
40. Algazi AP, Twitty CG, Tsai KK, Le M, Pierce R, Browning E, et al. Phase II trial of IL-12 plasmid transfection and PD-1 blockade in immunologically quiescent melanoma. Clin Cancer Res 2020;26:2827–37. https://doi.org/10.1158/1078-0432.Ccr-19-2217.
41. Sheinin M, Mondal S, Pahan K. Neutralization of p40 homodimer and p40 monomer leads to tumor regression in patient-derived xenograft mice with pancreatic cancer. Cancers (Basel) 2023;15:5796. https://doi.org/10.3390/cancers15245796.
42. Kundu M, Raha S, Roy A, Pahan K. Regression of triple-negative breast cancer in a patient-derived xenograft mouse model by monoclonal antibodies against IL-12 p40 monomer. Cells 2022;11:259. https://doi.org/10.3390/cells11020259.
43. Garris CS, Arlauckas SP, Kohler RH, Trefny MP, Garren S, Piot C, et al. Successful anti-PD-1 cancer immunotherapy requires T cell-dendritic cell crosstalk involving the cytokines IFN-γ and IL-12. Immunity 2018;49:1148–61.e7. https://doi.org/10.1016/j.immuni.2018.09.024.
44. Okamoto I, Kohno K, Tanimoto T, Ikegami H, Kurimoto M. Development of CD8+ effector T cells is differentially regulated by IL-18 and IL-12. J Immunol 1999;162:3202–11. https://doi.org/10.4049/jimmunol.162.6.3202.
45. Gosmann C, Frazer IH, Mattarollo SR, Blumenthal A. IL-18, but not IL-12, induces production of IFN-γ in the immunosuppressive environment of HPV16 E7 transgenic hyperplastic skin. J Invest Dermatol 2014;134:2562–9. https://doi.org/10.1038/jid.2014.201.
46. Sorensen EW, Gerber SA, Frelinger JG, Lord EM. IL-12 suppresses vascular endothelial growth factor receptor 3 expression on tumor vessels by two distinct IFN-gamma-dependent mechanisms. J Immunol 2010;184:1858–66. https://doi.org/10.4049/jimmunol.0903210.
47. Kundu M, Roy A, Pahan K. Selective neutralization of IL-12 p40 monomer induces death in prostate cancer cells via IL-12-IFN-γ. Proc Natl Acad Sci U S A 2017;114:11482–7. https://doi.org/10.1073/pnas.1705536114.
48. Thomas AS, Ma W, Wang Y. Ustekinumab for refractory colitis associated with immune checkpoint inhibitors. N Engl J Med 2021;384:581–3. https://doi.org/10.1056/NEJMc2031717.
49. Perez Del Nogal G, Patel N. Refractory checkpoint inhibitor colitis responsive to ustekinumab. ACG Case Rep J 2022;9:e00946. https://doi.org/10.14309/crj.0000000000000946.
50. Ghosh S, Feagan BG, Ott E, Gasink C, Godwin B, Marano C, et al. Safety of ustekinumab in inflammatory bowel disease: pooled safety analysis through 5 years in crohn's disease and 4 years in ulcerative colitis. J Crohns Colitis 2024;18:1091–101. https://doi.org/10.1093/ecco-jcc/jjae013.
51. Hailemichael Y, Johnson DH, Abdel-Wahab N, Foo WC, Bentebibel SE, Daher M, et al. Interleukin-6 blockade abrogates immunotherapy toxicity and promotes tumor immunity. Cancer Cell 2022;40:509–23.e6. https://doi.org/10.1016/j.ccell.2022.04.004.
52. Yang W, Wang Y, Wang T, Li C, Shi L, Zhang P, et al. Protective effects of IRG1/itaconate on acute colitis through the inhibition of gasdermins-mediated pyroptosis and inflammation response. Genes Dis 2023;10:1552–63. https://doi.org/10.1016/j.gendis.2022.05.039.
53. Wei SC, Meijers WC, Axelrod ML, Anang N-AAS, Screever EM, Wescott EC, et al. A genetic mouse model recapitulates immune checkpoint inhibitor-associated myocarditis and supports a mechanism-based therapeutic intervention. Cancer Discov 2021;11:614–25. https://doi.org/10.1158/2159-8290.Cd-20-0856.